Coronary artery stenting affects wall shear stress topological skeleton

Claudio Chiastra
PoliTo^BIOMed Lab, Department of Mechanical and Aerospace Engineering, Politecnico di Torino
Turin, Italy
claudio.chiastra@polito.it

Valentina Mazzi
PoliTo^BIOMed Lab, Department of Mechanical and Aerospace Engineering, Politecnico di Torino
Turin, Italy
valentina.mazzi@polito.it

Maurizio Lodi Rizzini
PoliTo^BIOMed Lab, Department of Mechanical and Aerospace Engineering, Politecnico di Torino
Turin, Italy
maurizio.lodirizzini@polito.it

Karol Calò
PoliTo^BIOMed Lab, Department of Mechanical and Aerospace Engineering, Politecnico di Torino
Turin, Italy
karol.calo@polito.it

Anna Corti
Laboratory of Biological Structure Mechanics (LaBS), Department of Chemistry, Materials and Chemical Engineering "Giulio Natta", Politecnico di Milano
Milan, Italy
anna.corti@polimi.it

Alessandro Acquasanta
PoliTo^BIOMed Lab, Department of Mechanical and Aerospace Engineering, Politecnico di Torino
Turin, Italy
alessandro.acquasanta@studenti.polito.it

Giuseppe De Nisco
PoliTo^BIOMed Lab, Department of Mechanical and Aerospace Engineering, Politecnico di Torino

Turin, Italy
giuseppe.denisco@polito.it

Davide Belliggiano
Cardiology Division, San Luigi Gonzaga University Hospital, Orbassano
Turin, Italy
d.belliggiano@gmail.com

Enrico Cerrato
Interventional Cardiology Unit, San Luigi Gonzaga University Hospital, Orbassano, and
Rivoli Infermi Hospital, Rivoli
Turin, Italy
enrico.cerrato@gmail.com

Diego Gallo
PoliTo[BIO]Med Lab, Department of Mechanical and Aerospace Engineering, Politecnico di
Torino
Turin, Italy
diego.gallo@polito.it

Umberto Morbiducci[1]
PoliTo[BIO]Med Lab, Department of Mechanical and Aerospace Engineering, Politecnico di
Torino
Turin, Italy
umberto.morbiducci@polito.it

ABSTRACT

Despite the important advancements in the stent technology for the treatment of diseased coronary

arteries, major complications still affect the post-operative long-term outcome. The stent-induced flow

disturbances, and especially the altered wall shear stress (WSS) profile at the strut level, play an important

role in the pathophysiological mechanisms leading to stent thrombosis (ST) and in-stent restenosis (ISR). In

this context, the analysis of the WSS topological skeleton is gaining more and more interest by extending

the current understanding of the association between local hemodynamics and vascular diseases. The

present study aims to analyze the impact that a deployed coronary stent has on the WSS topological

---

[1] Corresponding author.

skeleton. Computational fluid dynamics simulations were performed in three stented human coronary artery geometries reconstructed from clinical images. The selected cases presented stents with different designs (i.e., two contemporary drug eluting stents and one bioresorbable scaffold) and included regions with stent malapposition or overlapping. A recently proposed Eulerian-based approach was applied to analyze the WSS topological skeleton features. The results highlighted that the presence of single or multiple stents within a coronary artery markedly impacts the WSS topological skeleton. In particular, repetitive patterns of WSS divergence were observed at the luminal surface, highlighting a WSS contraction action exerted proximal to the stent struts and a WSS expansion action distal to the stent struts. This WSS action pattern was independent from the stent design. In conclusions, these findings could contribute to a deeper understanding of the hemodynamic-driven processes underlying ST and ISR.

KEYWORDS

Percutaneous coronary intervention, computational fluid dynamics, divergence, fixed points, manifolds

INTRODUCTION

Percutaneous coronary intervention (PCI) with drug eluting stent implantation is the gold standard endovascular treatment for patients suffering from coronary artery disease [1]. Contemporary stent platforms are made of cobalt-chromium or platinum-chromium, allowing for thinner stent struts (< 100 µm) and more flexibility than old-generation devices, while maintaining adequate radial strength [2,3]. These modern devices have reduced the incidence rate of stent thrombosis (ST) below 1 % after 1 year of intervention [4,5]. Conversely, the incidence rate of in-stent restenosis (ISR) still remains at 5-10 % [6]. Moreover, the period of ISR presentation is generally longer than

that of the old-generation devices and often extends several years beyond the

intervention [6]. To avoid late adverse events promoted by the persistence of the

metallic platforms in the coronary vessel (including late ST and ISR), bioresorbable

scaffolds, either based on a fully resorbable polymeric or metallic backbone, are

currently under development and clinical testing [2]. These devices provide temporary

mechanical support and drug delivery to the coronary vessel within 1 year after

implantation and completely resorb in the subsequent 1-2 years, restoring the normal

luminal diameter and vasomotor function [2,3]. Bioresorbable scaffolds present the

notable advantage of reducing the need of the long-term dual antiplatelet therapy and

allow for surgical revascularization, if needed [2]. As a counterpart, they present the

disadvantage that thicker struts are necessary to provide radial forces similar to the

contemporary drug eluting stents [2], with the consequent exacerbation of the local

flow disturbances. In this regard, in addition to systemic and biologic factors [6,7],

numerous studies have identified local blood flow disturbances at the stent strut level as

a key contributor for the ISR development [7,8]. In particular, a negative association

between baseline wall shear stress (WSS) and neointimal thickness at follow-up has

emerged in different clinical datasets [8]. However, the role of the altered WSS profile

on the pathophysiological mechanisms leading to ISR is still under investigation.

Moreover, the lack of endothelial coverage or delayed re-endothelialization observed in

consequence of thicker stent struts, such as in bioresorbable scaffolds, increases the risk

of thrombosis [9,10].

In this context, the analysis of the WSS topological skeleton, which is contributing to improve and extend the current understanding of the association between local hemodynamics and vascular diseases [11–14], could allow to better identify the biomechanical stimuli involved in clinical adverse events eventually leading to failure of stenting procedures. The WSS topological skeleton is composed by fixed points, where the WSS vanishes, and by manifolds, connecting fixed points [11,12]. Recently, an approach has been proposed for (i) the identification of WSS manifolds [12,15] and (ii) the quantitative analysis of the contraction/expansion action exerted by the shear forces on the endothelium [15–17], starting from the distribution of the WSS divergence on the arterial luminal surface. Using such a WSS divergence-based approach, evidences emerged that the variability of the WSS contraction/expansion action along the cardiac cycle is associated with wall degradation in the ascending thoracic aorta aneurysm [17], and is a predictor of the risk of long-term restenosis in the carotid bifurcation after endarterectomy [16]. Furthermore, the findings of a very recent longitudinal study focusing on coronary arteries indicated that the high variability in the WSS contraction/expansion action is a predictor of wall thickness change over time (a hallmark of atherosclerosis development), suggesting that both the WSS manifold dynamics along the cardiac cycle and the WSS magnitude concur to coronary atherosclerosis, acting as different hemodynamic stimuli [15]. Applied in a clinical setting, the high variability in the WSS contraction/expansion action added incremental predictive and discriminative capacity to area stenosis, virtual fractional flow reserve

and time-averaged WSS to identify intermediate coronary lesion site of subsequent myocardial infarction at 5-year follow-up [18].

Based on the above mentioned observations and on the direct link of the WSS topological skeleton features with near-wall flow stagnation, separation, and recirculation, which represent typical flow conditions of stented coronary arteries [11,12], in this study the impact that a deployed coronary stent has on the WSS topological skeleton is investigated. The possible involvement of WSS topological skeleton features in the processes leading to post-PCI complications is discussed. For this purpose, computational fluid dynamics (CFD) simulations are performed in stented human coronary artery models reconstructed from clinical images. The impact of three different stent designs (i.e., two contemporary drug eluting stents and one bioresorbable scaffold) and of stent positioning (i.e., malapposition and overlapping) on the WSS topological skeleton features is analyzed.

METHODS

Coronary artery geometries

Three cases (A-C) of pathological left anterior descending (LAD) coronary artery of patients suffering from coronary artery disease who underwent percutaneous coronary stent implantation were investigated (Fig. 1). Cases A and B were treated with cobalt-chromium drug-eluting stents at University Hospital Doctor Peset (Valencia, Spain) [19,20]. In case A, a 3.0x28 mm Xience Prime everolimus-eluting stent (Abbott Laboratories, Abbott Park, IL, USA) was implanted in the proximal portion of the LAD at the level of the first diagonal branch and a septal branch by means of the provisional

side branch stenting technique concluded by proximal optimization. The Xience Prime stent is characterized by an open cell peak-to-valley design and struts with square cross-section and thickness of 81 μm (Fig. 2A) [2]. In case B, two Endeavor Resolute zotarolimus-eluting stents (Medtronic, Dublin, Ireland) (sizes 2.75x15 mm and 3.0x15 mm) were deployed in the mid portion of the LAD in correspondence of the first and second diagonal branches. The two stents were sequentially deployed using the provisional side branch technique, ensuring a stent overlapping region of ~20 mm. The Endeavor Resolute stent presents an open cell peak-to-peak design and struts with circular cross-section and diameter of 91 μm (Fig. 2B) [2]. Case C was treated with a drug-eluting bioresorbable scaffold at Rivoli Infermi Hospital (Turin, Italy). In particular, a 3.0x25 mm resorbable magnesium-based sirolimus-eluting scaffold Magmaris (Biotronik AG, Bülach, Switzerland) was implanted in the mid portion of the LAD in correspondence of the second diagonal branch following a provisional stenting technique concluded by proximal optimization, without the need of final kissing balloon inflation. This bioresorbable scaffold is characterized by an open cell peak-to-valley design with mid-strut connector and struts with rectangular cross-section and thickness of 150 μm (Fig. 2C) [21]. The study was conducted in accordance with the principles of the Declaration of Helsinki and met the requirement of medical ethics. The study protocol was approved by the institutional review board of the involved hospitals. All patients gave written informed consent.

Patient-specific geometries of the three stented coronary arteries were obtained from medical images (Fig. 1). Regarding Cases A and B, pre-operative vessel geometries

were reconstructed by combining conventional angiography and computed tomography angiography images. Finite element analyses replicating the entire stenting procedure were then performed to obtain the stented lumen configuration (i.e., post-PCI vessel configuration) to be used for CFD simulations. Details on vessel and stent geometry reconstruction, and virtual stenting procedure were extensively described elsewhere [19,20]. Regarding Case C, the post-PCI vessel configuration was reconstructed through the fusion of conventional angiography and optical coherence tomography (OCT) images acquired immediately after scaffold implantation. More in detail, the following five-step procedure was applied [22–24]: (i) semi-automatic detection of the lumen contours and stent struts on the OCT frames using an in-house developed algorithm; (ii) extraction of the vessel centerline from two angiographic views; (iii) placement of the lumen contours and stent struts orthogonal to the vessel centerline using the side branches as reference to properly orient the OCT frames; (iv) smooth connection of the lumen contours to obtain the lumen surface; and (v) creation of the 3D stent model by means of a manual morphing procedure that adapts the stent skeleton in its straight free-expanded configuration towards the stent point cloud detected from OCT.

In addition to the three stented coronary artery geometries, the corresponding lumen geometries without stent (i.e., non-stented cases) were considered for comparison purposes. These vessel geometries were obtained by excluding the stents from the domain of interest and by smoothing the lumen surface using the open-source software VMTK (Orobix, Bergamo, Italy) to avoid abrupt local changes of the luminal surface after the stent removal.

Computational fluid dynamics

The coronary artery geometries were discretized into tetrahedral elements with 5 layers of prismatic elements at the luminal surface using the commercial software Fluent Meshing (Ansys Inc., Canonsburg, PA, USA). The element size was defined based on a mesh independence study, resulting in a mesh cardinality ranging from 5,068,182 to 13,948,023 elements and from 526,492 to 1,548,654 elements for the stented and non-stented vessel models, respectively. A smaller element size (0.02 mm) was defined at the stent struts.

The local hemodynamics of all cases under investigation was analyzed by performing transient CFD simulations. Specifically, the governing equations of the unsteady-state fluid motion were numerically solved using the finite volume-based commercial code Fluent (Ansys Inc.). Details on boundary conditions imposed at inlet and outlet sections of each model were extensively described in [19]. Briefly, a pulsatile flow waveform, distinctive for the LAD [25], was applied as paraboloid-shaped velocity profile at the inlet cross section [26]. The pulsatile flow waveform amplitude was personalized to the specific patient according to an inflow section lumen diameter-based scaling law [27]. In this way, flow rate waveforms with anatomically derived, personalized average flow rate values (42.2 mL/min, 45.1 mL/min and 34.0 mL/min for cases A, B and C, respectively) were prescribed as inflow boundary conditions (Fig S1 in Supplemental Materials). A flow-split, estimated through a scaling law based on the lumen diameter of the daughter branches [27], was imposed at the outflow boundaries (Fig S1 in Supplemental Materials). The no-slip condition was applied at the vessel and

9

stent walls, which were considered as rigid. The blood was modeled as an

incompressible, homogeneous, non-Newtonian fluid with density of 1060 kg/m^3 and

viscosity described through the Carreau formulation [19]. The flow was considered

laminar as the maximum Reynolds number at peak flow rate was 195, 260, and 140 for

cases A, B and C, respectively. Details on the numerical settings were exhaustively

reported in a previous study [19].

Wall shear stress features

The Eulerian-based method recently proposed for Newtonian fluids [12] and

extended to the class of Reiner-Rivlin fluids [15] was applied to analyze the WSS

topological skeleton features at the stented region, considered as the region of interest.

More in detail, the WSS topological skeleton consists of a collection of fixed points (i.e.,

focal points where the WSS vanishes) and associated unstable/stable manifolds [11,12]

(Fig. 3A). As reported in previous studies [12,15], WSS manifolds can be identified by

computing the divergence of the normalized WSS vector field at the stented vessel

surface, expressed as:

$$\mathrm{DIV_{WSS}} = \nabla \cdot \left(\frac{\boldsymbol{\tau}}{\|\boldsymbol{\tau}\|_2} \right) = \nabla \cdot \boldsymbol{\tau}_u, \tag{1}$$

where $\boldsymbol{\tau}$ and $\boldsymbol{\tau}_u$ are the WSS vector and its unit vector, respectively. From a physical

perspective, vessel surfaces characterized by negative/positive values of $\mathrm{DIV_{WSS}}$

correspond to contraction/expansion regions approximating unstable/stable manifolds

(Fig. 3A). To complete the WSS topological skeleton analysis, the WSS fixed points were

identified at the vessel surface according to the procedure proposed elsewhere, based on

the Poincaré index [11,12,28]. Then, the WSS fixed points were classified according to their nature (i.e., saddle point, node or focus – Fig. 3A), using the approach based on the eigenvalues of the WSS Jacobian matrix [11–13,29].

First, the cycle-average WSS vector field $\bar{\tau}$ was analyzed. Subsequently, the instantaneous WSS topological skeleton along the cardiac cycle was characterized. To do that, the amount of variation in the WSS contraction or expansion action along the cardiac cycle (Fig. 2B) was quantified by computing the topological shear variation index (TSVI) [15–17], namely the root mean square deviation of the divergence of the normalized WSS with respect to its average along the cardiac cycle:

$$\text{TSVI} = \left\{ \frac{1}{T} \int_0^T \left[\nabla \cdot (\boldsymbol{\tau}_u) - \overline{\nabla \cdot (\boldsymbol{\tau}_u)} \right]^2 dt \right\}^{1/2},$$ (2)

where T is the cardiac cycle period. Moreover, to characterize the unsteady nature of the WSS fixed points along the cardiac cycle, the WSS fixed point weighted residence time along the cardiac cycle was computed [12,15,16]:

$$\text{RTV}_{\text{x}_{\text{fp}}}(e) = \frac{A_{avg}}{A_e} \frac{1}{T} \int_0^T \mathbb{I}_e\big(\boldsymbol{x}_{fp}, t\big) \, |(\nabla \cdot \boldsymbol{\tau})_e| \, dt,$$ (3)

where $\boldsymbol{x}_{fp}(t)$ represents the location of a WSS fixed point at time t $\in [0, T]$, e is a generic element of the mesh of area A_e, A_{avg} the average surface area of all elements of the mesh, $\mathbb{I}$ is the indicator function and $(\nabla \cdot \boldsymbol{\tau})_e$ is the instantaneous WSS divergence. Eq. (3) quantifies the fraction of cardiac cycle in which a generic mesh element e hosts a fixed point, weighting the residence time by the strength of the contraction/expansion action measured by the WSS divergence.

11

To provide a more complete picture of the near-wall hemodynamics, the well-known WSS-based descriptor time-averaged WSS (TAWSS), namely the average WSS magnitude value along the cardiac cycle, was computed in addition to the WSS topological skeleton features.

The exposure to large variations in the WSS contraction or expansion action was quantified by the relative surface area at the stented region exposed to high values of TSVI, considering as threshold value the 80th percentile of the TSVI distribution of each non-stented model. This variable was denoted as topological shear variation area (TSVA). Similarly, the exposure to the action of instantaneous WSS fixed points was quantified by the relative surface area exposed to non-null values of $\mathrm{RT}\nabla_{\mathrm{x_{fp}}}(e)$, namely considering the luminal surface area at the stented region where fixed points occurred along the cardiac cycle. This variable was denoted as weighted fixed point area (wFPA). Finally, the exposure to low TAWSS values was quantified by the relative surface area at the stented region exposed to TAWSS values below a threshold value, corresponding to the 20th percentile of the TAWSS distribution of the non-stented model. This variable was denoted as low shear area (LSA).

RESULTS

Hemodynamic impact of stenting

Since the WSS topological skeleton features directly link to near-wall flow stagnation, separation, and recirculation areas [11,12], an overview of the intravascular hemodynamic features of the three cases under analysis is briefly presented in Fig. 4,

comparing the stented with the non-stented models in terms of in-plane flow patterns on explanatory cross-sectional planes. As expected, stent implantation induced small flow recirculation regions close to the stent struts, whose extension was dictated by the peculiar design features of the stent. In these explanatory cases, the near-wall recirculation regions did not affect the large-scale secondary flow patterns, except for Case C, where the stent struts broke the classical two-vortex Dean-like structure of the secondary flows.

The differences in the hemodynamics induced by the implantation of stents with different design were reflected by the WSS topological skeleton features. The cycle average WSS topological skeleton distribution at the luminal surface of the three cases under investigation, expressed in terms of divergence of the normalized WSS vector field, is displayed in Fig. 5. By visual inspection, in all three cases the presence of the stent markedly impacted the WSS topological skeleton. In particular, the stented regions presented a repetitive pattern characterized by WSS contraction regions located immediately upstream from each stent ring, identified by negative DIV_{WSS} values, and WSS expansion regions located immediately downstream from each stent ring, identified by positive DIV_{WSS} values. This repetitive pattern was observed along the entire stented regions, except for the stent malapposed region (i.e., proximal stented segment of Case A), where a reverse DIV_{WSS} distribution was visible, and the stent overlapped region (i.e., mid stented segment of Case B), where a less repetitive pattern was present. The bifurcation regions of the stented cases showed a more complex WSS topological skeleton distribution than that of the non-stented cases, in which only a WSS

expansion region was identified at the bifurcations' carina. In the stented cases, WSS

fixed points were mainly located at the stent peaks and valleys, at the interface between

the lumen and the stent struts. The number of fixed points was at least two orders of

magnitude higher than that of the non-stented cases (Table 1), for which only a single

(Case A) or few saddle points (Cases B and C) were present at the bifurcation regions.

Consequently, a high percentage increase (> 70%) in the wFPA was also observed in the

stented cases with respect to the non-stented ones (Table 2).

The distribution of TSVI along the luminal surface of the stented cases was

different than that of the non-stented ones (Fig. 6). Specifically, in the stented cases

marked variations in the WSS contraction/expansion action along the cardiac cycle, as

quantified by TSVI, were mainly located immediately downstream and upstream from

the stent struts. The highest values of TSVI (> 5000 m^{-1}) were found at the stent peaks

and valleys, and at the links between the stent rings. Conversely, in the non-stented

cases high TSVI values were located only at the bifurcation regions and at the proximal

segment of Case A, where the coronary artery presented high curvature and tortuosity.

The difference in the distributions of TSVI along the luminal surface between the

stented and non-stented cases emerged also from the violin plots of Fig. 7. The stented

cases were characterized by higher median values of TSVI as compared to the non-

stented ones (862.79 m^{-1} versus 92.53 m^{-1}, 802.78 m^{-1} versus 102.69 m^{-1}, and 662.97 m^{-1}

versus 119.18 m^{-1}, for the stented versus the non-stented models of Case A, B and C,

respectively). Furthermore, the stent presence caused a marked percentage increase (>

550%) in the TSVA (Table 2).

The distribution of TAWSS along the luminal surface of the stented cases was different than that of the non-stented ones, as visually emerged from the color maps of Fig. 8 and the corresponding violin plots of Fig. 9. In both the stented and non-stented cases, low TAWSS values were located at the bifurcation regions and at the proximal segment of Case A. In the stented cases, low TAWSS were also present at the stent struts, as expected. The median values of TAWSS were lower in the case of the stented models as compared to the non-stented ones (0.54 Pa versus 1.02 Pa, 0.57 Pa versus 0.93 Pa, and 0.45 Pa versus 0.76 Pa, for the stented versus the non-stented models of Case A, B and C, respectively). The LSA was markedly higher in the case of the stented models with respect to the non-stented ones (percentage increase > 400% in all cases, Table 2). Moreover, by comparing the color maps of TSVI and TAWSS of Figs. 5 and 7, a co-localization between high TSVI and low TAWSS values in the vicinity of the stent struts was observable.

The distributions of DIV_{WSS}, TSVI and TAWSS on the stent surface are depicted in Fig. 10 for the three investigated stents. A continuous DIV_{WSS} distribution can be observed between the luminal surface close to the stent struts and their side faces (i.e., negative and positive DIV_{WSS} values for the proximal and distal lateral surfaces of the stent struts at the intersection with the luminal surface, respectively). A transition from positive to negative DIV_{WSS} values (i.e., from WSS expansion to contraction regions) in the main flow direction was identified at the top faces of the stent struts. The highest values of TSVI co-localized with the lowest values of TAWSS at the stent peaks and

valleys. Low values of TSVI and high values of TAWSS were present at the top faces of the stent struts.

Impact of stent design

The repetitive pattern of the cycle average WSS topological skeleton distribution at the luminal surface, characterized by WSS contraction regions located upstream of the stent rings, and WSS expansions regions located downstream from the stent rings, was present in all the investigated cases (Fig. 5), suggesting that this pattern was independent from the stent design features. A different number of fixed points was found in the three investigated cases (Table 1). The number of fixed points depended from the number of peaks/valleys per stent ring and the stent length. The higher the number of peaks/valleys per stent ring and the longer the stent length, the higher the number of fixed points. Consequently, the highest number of fixed points was identified in Case B, where two Endeavor Resolute stents were implanted (total length of ~28 mm, 10 peaks per stent rings), while the lowest number in Case C, where the Magmaris stent was deployed (length of 25 mm, 6 peaks per stent rings). Accordingly, the highest percentage increase (440.16 %) in the wFPA was observed in Case B, while the lowest (71.07%) in Case C (Table 2). The number of saddle points and foci/nodes was balanced only in case C (Table 1). Conversely, the number of saddle points was lower than that of the foci/nodes in Case A and higher than that of the foci/nodes in Case C (Table 1).

The distributions of TSVI along the luminal surfaces of the stented regions were similar for the three investigated cases (Figs. 6 and 7). Although the general patterns of

16

the TAWSS along the stented region were similar for the different cases (i.e., low TAWSS close to the stent struts, gradually increasing towards the stent cell center, Fig. 8), the TAWSS median value for Case C was lower than that of the other two cases (0.45 Pa versus 0.54 Pa and 0.57 Pa for Case C versus Cases A and B, respectively, Fig. 9), suggesting that the open-cell design of the Magmaris stent, characterized by thicker struts than the Xience Prime and Endevour Resolute stents, had a higher impact on the TAWSS distribution.

DISCUSSION

Summary of findings

The present study investigated the impact that the stenting of human coronary arteries has on the WSS topological skeleton, whose features highlight the complex nature of the interaction of fluid shear forces with the stent struts and the luminal surface. Transient CFD simulations were performed in three patient-specific coronary models featuring different implanted stents, namely two contemporary drug eluting stents and one bioresorbable scaffold. The WSS topological skeleton features were analyzed along the stented regions by applying a recently proposed Eulerian-based method [12,15]. The results of the work demonstrated that the presence of single or multiple stents within a coronary artery highly impacts the WSS vector field topological skeleton. More specifically, first a repetitive pattern of the WSS topological skeleton distribution at the luminal surface was observed in the stented regions of all investigated cases. As schematized in Fig. 11, this pattern was characterized by a WSS contraction action on the luminal surface (negative DIV_{WSS} values) immediately

17

proximal to the stent struts and by a WSS expansion action (positive DIV_{WSS} values) immediately distal to the stent struts. Second, this pattern was independent of the stent design, stent strut cross-section shape and thickness. Third, the highest variations in the WSS contraction/expansion action exerted on luminal surface interacting with the streaming blood along the cardiac cycle, as captured by the TSVI, were located close to the stent struts. Last, high TSVI co-localized with low TAWSS values in the vicinity of the stent struts.

WSS topological skeleton and post-PCI complications

Despite the advancements in the stent technology, ST and ISR are major adverse events still affecting the post-PCI long-term outcome [8]. The stent-induced flow disturbances, and more specifically the altered WSS patterns at the stent strut level, play an important role in the pathophysiological mechanisms leading to ST and ISR [7,8]. In this context, this work extends the current knowledge on the impact of stent implantation on local hemodynamics, presenting for the first time the characterization of the WSS topological skeleton in human stented coronary arteries. Motivated by recent studies highlighting the influence that peculiar WSS topological skeleton features have on vascular adverse events (i.e, wall degradation in the ascending thoracic aorta aneurysm [17], long-term restenosis in the carotid bifurcation after endarterectomy [16], and wall thickness change over time in coronary arteries prone to atherosclerotic lesion development [15]), the analysis here proposed could represent an important starting point for better elucidating the role of altered WSS profiles in promoting ST and

ISR in stented arteries. Moreover, we have recently demonstrated the feasibility of a comprehensive diagnostic approach that includes WSS topological skeleton analysis in a conventional clinical framework to stratify the risk of myocardial infarction in patients with mild coronary lesions [18], holding the promise of a future extension to other clinical applications such as stented coronary arteries.

PCI with stenting causes severe vascular injury producing endothelial denudation [30]. A process of re-endothelization begins immediately after stent deployment leading to the repopulation of the damaged endothelium in the weeks after intervention through the proliferation of the endothelial cells remaining within the stented portion, of those close to the treated lesion, and of circulating endothelial progenitor from the blood [30–32]. This process can be incomplete or, even if endothelium is completely restored, it can be dysfunctional, thus resulting in impaired endothelial function [30]. Incomplete endothelium promotes the insurgence of ST by exposing potential thrombogenic material, such as the stent material, to the circulating prothrombotic factors [10,30]. Incomplete and dysfunctional endothelium represents a major factor promoting the development of ISR through the increase in permeability, in the expression of chemotactic molecules, in the recruitment and accumulation of monocytes and macrophages, in the smooth muscle cell proliferation and migration, and in the expression of procoagulatory molecules [33–35]. Re-endothelialization rates are affected by the local hemodynamic environment of the stented arterial segment, in particular by the WSS patterns at the stent strut level [9,10]. Low WSS is known to (i) attenuate the endothelial production of nitric oxide, prostacyclin I_2, and tissue

plasminogen activator, and (ii) inhibit endothelial cell proliferation and delay re-endothelialization [7]. The present study confirms evidence from literature [7,8,19,36]: luminal regions close to the stent struts exhibit low WSS, as emerged from the distributions of TAWSS of the three investigated cases (Fig. 8). Additionally, it shows that (i) the luminal regions upstream of the stent struts are characterized by WSS contraction while those downstream of the stent struts by WSS expansion (Fig. 5), and (ii) both these luminal regions are characterized by high TSVI (i.e., high variations in the WSS contraction or expansion action along the cardiac cycle) (Fig. 6). The presence of WSS contraction/expansion regions upstream/downstream of the stent struts may contribute to explain the preferential migration direction of endothelial cells, which were shown, at least in an *in vitro* experiment [37], to migrate in the direction of the flow upstream of the stent struts and to accumulate downstream of the stent struts, being entrapped at the recirculation zone behind the stent struts. Furthermore, the high variability of the WSS manifolds along the cardiac cycle may lead to the dysfunction of the cells in contact with blood immediately post-PCI, namely the remaining endothelial cells and the smooth muscle cells (usually not in contact with the blood), by exerting a push/pull action on those cells.

ST can be induced by high WSS values, which can lead to platelet activation and triggering of the coagulation cascade [7,8]. High stent strut thickness (e.g., ≥ 150 μm as in the case of the current bioresorbable scaffolds, such as the Magmaris scaffold of Case C) is associated with increased risk of ST [3,7,8,10]. This study confirms that high TAWSS are present at the stent strut top face (Fig. 10), in agreement with previous studies [7,8].

Furthermore, it highlights that the stent strut top face exhibits high variability in the WSS contraction/expansion action (Fig. 10). Further investigation is recommended to elucidate the role of the WSS topological skeleton features on the mechanisms triggering ST.

ST and ISR seem to be favored by inadequate stent positioning, including the conditions of stent malapposition (e.g., proximal stented segment of Case A) and stent overlapping (e.g., mid stented segment of Case B) [7,8,38]. Interestingly, a different DIV_{WSS} luminal distribution was observed in these regions as compared to those featuring well-apposed stent struts (Fig. 5). Again, further investigation is required to better understand the role of the identified WSS topological skeleton features on the underlying mechanisms of ST and ISR.

Impact of stent design

Previous *in silico*, *in vitro* and *in vivo* investigations have demonstrated that the stent design (e.g., closed-cell vs. open-cell stent design, stent strut cross-section shape and thickness, strut connector length) has a strong impact on the local hemodynamics, which in turn may influence the vessel response to stenting, potentially triggering ST or ISR [7,8]. In this study, the impact of three stents with different design (peak-to-valley for the Xience Prime and Magmaris stents of Cases A and C, respectively, and peak-to-peak for Endeavor Resolute stents of Case B), strut cross-section shape (square, circular and rectangular cross-section shape for the Xience Prime, Endeavor Resolute and Magmaris stents, respectively) and thickness (81μm, 91 μm, and 150 μm for the Xience

Prime, Endeavor Resolute and Magmaris stents, respectively) on the WSS topological

skeleton features was analyzed. Despite the differences in the design of the three

considered stent platforms, a similar repetitive pattern of the WSS topological skeleton

distribution was observed at the luminal surface of the stented region in all cases (Fig.

5). However, the number of fixed points of each case was different and depended on (i)

the number of peaks/valleys per stent ring and (ii) the stent length. Case B presented

the highest number of fixed points, as the implanted Endeavor Resolute stents were

characterized by the highest number of peaks per stent ring as compared to the other

stent design and by the longest total stent length. The TSVI distribution at the luminal

surface was similar in all cases (Fig. 6), suggesting that the highest variations in the WSS

manifolds along the cardiac cycle are located close to the stent struts independent of

the stent design. From a quantitative viewpoint, Case C, in which the Magmaris scaffold

was deployed, presented lower median values of both TSVI and TAWSS than the other

two cases. The lower median values of TAWSS could be explained by the square strut

cross-section of the Magmaris scaffold presenting with higher thickness than the other

two stent designs [7,39,40]. In order to draw definitive conclusions, a dedicated

comparative analysis should be conducted on an idealized vessel geometry with

different implanted stents to systematically quantify the effect of the stent design

parameters (e.g., stent strut thickness) on the WSS topological skeleton features,

without considering the influence of the patient-specific vessel geometry and boundary

conditions on the hemodynamic results.

Limitations

22

This study faces some limitations. Only three image-based stented coronary artery models were considered herein. A large number of cases, including different stent designs, stent malapposition and stent overlapping regions, should be analyzed to provide more general conclusions. Regarding the CFD models, in the absence of patient-specific flow measurements, boundary conditions were derived from: a diameter-based scaling law applied at the outflow sections [27]; a characteristic pulsatile flow waveform available from the literature [25], whose amplitude was scaled to the diameter of the inflow section [27]. This allowed prescribing boundary conditions that were personalized with respect to the specific anatomical features of each case. The flow rate values at the inflow section were then imposed in terms of Dirichlet boundary condition by prescribing a parabolic velocity profile. We have recently demonstrated that the influence of the velocity profile shape imposed at the inflow section is limited to a very few diameter lengths in computational hemodynamic models of LADs [26]; thus, we expect here a small effect of the inflow velocity profile on the WSS distribution at stented regions. In general, the adopted boundary conditions might have some impact on the in-stent WSS topological skeleton features. However, at this stage of the investigation the lack of measured patent-specific inflow rate waveforms does not entail the generality of the results, at least in terms of the localization of the WSS contraction and expansion regions, as by construction the WSS topological skeleton analysis is based on the normalized WSS. Moreover, the vessel and stent walls were assumed as rigid based on a previous fluid-structure interaction work highlighting that the rigid-wall assumption has marginal effect on the WSS distribution of a stented coronary artery

23

model [41]. Finally, the coronary artery motion during the cardiac cycle was neglected. Previous computational findings suggested that the cardiac-induced motion in untreated coronary arteries has a moderate impact on the coronary flow and WSS distribution [42]. Nevertheless, further investigation is required to confirm these findings in the case of stented coronary arteries when analyzing the WSS topological skeleton features.

CONCLUSIONS

In this study, a recently developed Eulerian-based method [12,15] was used to characterize the WSS topological skeleton of human stented coronary arteries. The findings of the study revealed that the presence of single or multiple stents within a coronary artery severely affects the WSS topological skeleton features. The high variability in the WSS contraction/expansion action exerted at the luminal surface close to the stent struts may have important implications in the pathophysiological mechanisms leading to ST and ISR. These findings contribute to a deeper understanding of the hemodynamic-driven processes underlying ST and ISR, stimulating further investigations in order to elucidate the link between the WSS topological skeleton features and post-PCI complications.

ACKNOWLEDGMENT

FUNDING

CONFLICTS OF INTEREST

The authors declare that they have no conflict of interest.

AUTHORS' CONTRIBUTIONS

Conceptualization: C.C., V.M., D.G., U.M.; Data Curation: C.C., V.M., D.B., E.C.; 3D stented vessel reconstruction: C.C., M.L.R.; Meshing: V.M., A.C., A.A.; Simulations: V.M., A.A.; Post-processing of the results: V.M.; Interpretation of data: C.C., V.M., E.C., D.G., U.M.; Writing – Original Draft Preparation: C.C., V.M.; Writing – Review & Editing: C.C., V.M., M.L.R., K.C., A.C., A.A., G.D.N., D.B., E.C., D.G., U.M. All authors discussed the results and reviewed the manuscript.

NOMENCLATURE

PCI	Percutaneous coronary intervention
ST	Stent thrombosis
ISR	In-stent restenosis
WSS	Wall shear stress
CFD	Computational fluid dynamics
LAD	Left anterior descending coronary artery
OCT	Optical coherence tomography
DIV_{WSS}	Divergence of normalized wall shear stress
TSVI	Topological shear variation index
$RT\nabla_{x_{fp}}(e)$	WSS fixed point weighted residence time
TAWSS	Time-averaged wall shear stress
TSVA	Topological shear variation area
wFPA	Weighted fixed point area
LSA	Low shear area

REFERENCES

[1]   Otake, H., 2021, "Stent Edge Restenosis - An Inevitable Drawback of Stenting?," Circ. J. Off. J. Japanese Circ. Soc., **85**(11), pp. 1969–1971.

[2]   Tomberli, B., Mattesini, A., Baldereschi, G. I., and Di Mario, C., 2018, "A Brief History of Coronary Artery Stents," Rev. Española Cardiol. (English Ed., **71**(5), pp. 312–319.

[3]   Stefanini, G., Byrne, R., Windecker, S., and Kastrati, A., 2017, "State of the Art: Coronary Artery Stents - Past, Present and Future," EuroIntervention, **13**(6), pp. 706–716.

[4]   Reejhsinghani, R., and Lotfi, A. S., 2015, "Prevention of Stent Thrombosis: Challenges and Solutions," Vasc. Health Risk Manag., **11**, p. 93.

[5]   Byrne, R. A., Joner, M., and Kastrati, A., 2015, "Stent Thrombosis and Restenosis: What Have We Learned and Where Are We Going? The Andreas Grüntzig Lecture ESC 2014," Eur. Heart J., **36**(47), p. 3320.

[6]   Shlofmitz, E., Iantorno, M., and Waksman, R., 2019, "Restenosis of Drug-Eluting Stents: A New Classification System Based on Disease Mechanism to Guide Treatment and State-of-the-Art Review," Circ. Cardiovasc. Interv., **12**(8), p. e007023.

[7]   Koskinas, K. C., Chatzizisis, Y. S., Antoniadis, A. P., and Giannoglou, G. D., 2012, "Role of Endothelial Shear Stress in Stent Restenosis and Thrombosis: Pathophysiologic Mechanisms and Implications for Clinical Translation," J. Am. Coll. Cardiol., **59**(15), pp. 1337–1349.

[8]   Ng, J., Bourantas, C. V., Torii, R., Ang, H. Y., Tenekecioglu, E., Serruys, P. W., and Foin, N., 2017, "Local Hemodynamic Forces after Stenting: Implications on Restenosis and Thrombosis," Arterioscler. Thromb. Vasc. Biol., **37**(12), pp. 2231–2242.

[9]   Kolandaivelu, K., Swaminathan, R., Gibson, W. J., Kolachalama, V. B., Nguyen-Ehrenreich, K. L., Giddings, V. L., Coleman, L., Wong, G. K., and Edelman, E. R., 2011, "Stent Thrombogenicity Early in High-Risk Interventional Settings Is Driven by Stent Design and Deployment and Protected by Polymer-Drug Coatings," Circulation, **123**(13), pp. 1400–1409.

[10]   Nguyen, D. T., Smith, A. F., and Jiménez, J. M., 2021, "Stent Strut Streamlining and Thickness Reduction Promote Endothelialization," J. R. Soc. Interface, **18**(181), p. 20210023.

[11]   Mazzi, V., Morbiducci, U., Calò, K., De Nisco, G., Lodi Rizzini, M., Torta, E., Caridi, G. C. A., Chiastra, C., and Gallo, D., 2021, "Wall Shear Stress Topological Skeleton Analysis in Cardiovascular Flows: Methods and Applications," Mathematics, **9**(7), p. 720.

[12]   Mazzi, V., Gallo, D., Calò, K., Najafi, M., Khan, M. O., De Nisco, G., Steinman, D. A., and Morbiducci, U., 2019, "A Eulerian Method to Analyze Wall Shear Stress Fixed Points and Manifolds in Cardiovascular Flows," Biomech. Model. Mechanobiol., **9**(5), pp. 1403–1423.

[13]   Arzani, A., and Shadden, S. C., 2018, "Wall Shear Stress Fixed Points in Cardiovascular Fluid Mechanics," J. Biomech., **73**, pp. 145–152.

[14]   Arzani, A., Gambaruto, A. M., Chen, G., and Shadden, S. C., 2016, "Lagrangian Wall Shear Stress Structures and Near-Wall Transport in High-Schmidt-Number Aneurysmal Flows," J. Fluid Mech., **790**, pp. 158–172.

[15]   Mazzi, V., De Nisco, G., Hoogendoorn, A., Calò, K., Chiastra, C., Gallo, D., Steinman, D. A., Wentzel, J. J., and Morbiducci, U., 2021, "Early Atherosclerotic Changes in Coronary Arteries Are Associated with Endothelium Shear Stress Contraction/Expansion Variability," Ann. Biomed. Eng., **49**(9), pp. 2606–2621.

[16]   Morbiducci, U., Mazzi, V., Domanin, M., De Nisco, G., Vergara, C., Steinman, D. A., and Gallo, D., 2020, "Wall Shear Stress Topological Skeleton Independently Predicts Long-Term Restenosis after Carotid Bifurcation Endarterectomy," Ann. Biomed. Eng., **48**(12), pp. 2936–2949.

[17]   De Nisco, G., Tasso, P., Calò, K., Mazzi, V., Gallo, D., Condemi, F., Farzaneh, S., Avril, S., and Morbiducci, U., 2020, "Deciphering Ascending Thoracic Aortic Aneurysm Hemodynamics in Relation to Biomechanical Properties," Med. Eng. Phys., **82**, pp. 119–129.

[18]   Candreva, A., Pagnoni, M., Rizzini, M. L., Mizukami, T., Gallinoro, E., Mazzi, V., Gallo, D., Meier, D., Shinke, T., Aben, J. P., Nagumo, S., Sonck, J., Munhoz, D., Fournier, S., Barbato, E., Heggermont, W., Cook, S., Chiastra, C., Morbiducci, U., De Bruyne, B., Muller, O., and Collet, C., 2021, "Risk of Myocardial Infarction Based on Endothelial Shear Stress Analysis Using Coronary Angiography," Atherosclerosis, In press. doi: 10.1016/j.atherosclerosis.2021.11.010

[19]   Chiastra, C., Morlacchi, S., Gallo, D., Morbiducci, U., Cárdenes, R., Larrabide, I., and Migliavacca, F., 2013, "Computational Fluid Dynamic Simulations of Image-Based Stented Coronary Bifurcation Models.," J. R. Soc. Interface, **10**(84), p. 20130193.

[20]   Morlacchi, S., Colleoni, S. G., Cárdenes, R., Chiastra, C., Diez, J. L., Larrabide, I., and Migliavacca, F., 2013, "Patient-Specific Simulations of Stenting Procedures in Coronary Bifurcations: Two Clinical Cases.," Med. Eng. Phys., **35**(9), pp. 1272–81.

[21]   Cerrato, E., Barbero, U., Gil Romero, J. A., Quadri, G., Mejia-Renteria, H., Tomassini, F., Ferrari, F., Varbella, F., Gonzalo, N., and Escaned, J., 2019, "Magmaris^TM Resorbable Magnesium Scaffold: State-of-Art Review," Future Cardiol., **15**(4), pp. 267–279.

[22]   Chiastra, C., Montin, E., Bologna, M., Migliori, S., Aurigemma, C., Burzotta, F., Celi, S., Dubini, G., Migliavacca, F., and Mainardi, L., 2017, "Reconstruction of Stented

Coronary Arteries from Optical Coherence Tomography Images: Feasibility, Validation, and Repeatability of a Segmentation Method," PLoS One, **12**(6), p. e0177495.

[23] Migliori, S., Chiastra, C., Bologna, M., Montin, E., Dubini, G., Aurigemma, C., Fedele, R., Burzotta, F., Mainardi, L., and Migliavacca, F., 2017, "A Framework for Computational Fluid Dynamic Analyses of Patient-Specific Stented Coronary Arteries from Optical Coherence Tomography Images," Med. Eng. Phys., **47**, pp. 105–116.

[24] Chiastra, C., Migliori, S., Burzotta, F., Dubini, G., and Migliavacca, F., 2018, "Patient-Specific Modeling of Stented Coronary Arteries Reconstructed from Optical Coherence Tomography: Towards a Widespread Clinical Use of Fluid Dynamics Analyses," J. Cardiovasc. Transl. Res., **11**(2), pp. 156–172.

[25] Davies, J. E., Whinnett, Z. I., Francis, D. P., Manisty, C. H., Aguado-Sierra, J., Willson, K., Foale, R. a., Malik, I. S., Hughes, A. D., Parker, K. H., and Mayet, J., 2006, "Evidence of a Dominant Backward-Propagating 'Suction' Wave Responsible for Diastolic Coronary Filling in Humans, Attenuated in Left Ventricular Hypertrophy," Circulation, **113**(14), pp. 1768–1778.

[26] Lodi Rizzini, M., Gallo, D., De Nisco, G., D'Ascenzo, F., Chiastra, C., Bocchino, P. P., Piroli, F., De Ferrari, G. M., and Morbiducci, U., 2020, "Does the Inflow Velocity Profile Influence Physiologically Relevant Flow Patterns in Computational Hemodynamic Models of Left Anterior Descending Coronary Artery?," Med. Eng. Phys., **82**, pp. 58–69.

[27] van der Giessen, A. G., Groen, H. C., Doriot, P.-A., de Feyter, P. J., van der Steen, A. F. W., van de Vosse, F. N., Wentzel, J. J., and Gijsen, F. J. H., 2011, "The Influence of Boundary Conditions on Wall Shear Stress Distribution in Patients Specific Coronary Trees.," J. Biomech., **44**(6), pp. 1089–95.

[28] Garth, C., Tricoche, X., and Scheuermann, G., 2004, "Tracking of Vector Field Singularities in Unstructured 3D Time-Dependent Datasets," *IEEE Visualization 2004*, pp. 329–336.

[29] Gambaruto, A. M., and João, A. J., 2012, "Computers & Fluids Flow Structures in Cerebral Aneurysms," Comput. Fluids, **65**, pp. 56–65.

[30] Cornelissen, A., and Vogt, F. J., 2019, "The Effects of Stenting on Coronary Endothelium from a Molecular Biological View: Time for Improvement?," J. Cell. Mol. Med., **23**(1), pp. 39–46.

[31] Asahara, T., Masuda, H., Takahashi, T., Kalka, C., Pastore, C., Silver, M., Kearne, M., Magner, M., and Isner, J. M., 1999, "Bone Marrow Origin of Endothelial Progenitor Cells Responsible for Postnatal Vasculogenesis in Physiological and Pathological Neovascularization," Circ. Res., **85**(3), pp. 221–228.

[32] Lindner, V., Majack, R. A., and Reidy, M. A., 1990, "Basic Fibroblast Growth Factor Stimulates Endothelial Regrowth and Proliferation in Denuded Arteries," J. Clin.

Invest., **85**(6), pp. 2004–2008.

[33]   Van der Heiden, K., Gijsen, F. J. H., Narracott, A., Hsiao, S., Halliday, I., Gunn, J., Wentzel, J. J., and Evans, P. C., 2013, "The Effects of Stenting on Shear Stress: Relevance to Endothelial Injury and Repair," Cardiovasc. Res., **99**(2), pp. 269–75.

[34]   Chiu, J.-J., and Chien, S., 2011, "Effects of Disturbed Flow on Vascular Endothelium: Pathophysiological Basis and Clinical Perspectives.," Physiol. Rev., **91**(1), pp. 327–387.

[35]   Munk, P. S., Butt, N., and Larsen, A. I., 2011, "Endothelial Dysfunction Predicts Clinical Restenosis after Percutaneous Coronary Intervention," Scand. Cardiovasc. J., **45**(3), pp. 139–145.

[36]   Beier, S., Ormiston, J., Webster, M., Cater, J., Norris, S., Medrano-Gracia, P., Young, A., and Cowan, B., 2016, "Hemodynamics in Idealized Stented Coronary Arteries: Important Stent Design Considerations," Ann. Biomed. Eng., **44**(2), pp. 315–329.

[37]   Hsiao, S. T., Spencer, T., Boldock, L., Prosseda, S. D., Xanthis, I., Tovar-Lopez, F. J., Beusekom, H. M. M. Van, Khamis, R. Y., Foin, N., Bowden, N., Hussain, A., Rothman, A., Ridger, V., Halliday, I., Perrault, C., Gunn, J., and Evans, P. C., 2016, "Endothelial Repair in Stented Arteries Is Accelerated by Inhibition of Rho-Associated Protein Kinase," Cardiovasc. Res., **112**(3), pp. 689–701.

[38]   Lagache, M., Coppel, R., Finet, G., Derimay, F., Pettigrew, R. I., Ohayon, J., and Malvè, M., 2021, "Impact of Malapposed and Overlapping Stents on Hemodynamics: A 2D Parametric Computational Fluid Dynamics Study," Mathematics, **9**(8), p. 795.

[39]   Jiménez, J. M., and Davies, P. F., 2009, "Hemodynamically Driven Stent Strut Design," Ann. Biomed. Eng., **37**(8), pp. 1483–1494.

[40]   Tarrahi, I., Colombo, M., Hartman, E., Forero, M. T., Torii, R., Chiastra, C., Daemen, J., and Gijsen, F., 2020, "Impact of Bioresorbable Scaffold Design Characteristics on Local Haemodynamic Forces: An Ex Vivo Assessment with Computational Fluid Dynamics Simulations," EuroIntervention, **16**(11), pp. E930–E937.

[41]   Chiastra, C., Migliavacca, F., Martinez, M. A., and Malve, M., 2014, "On the Necessity of Modelling Fluid-Structure Interaction for Stented Coronary Arteries," J. Mech. Behav. Biomed. Mater., **34**, pp. 217–230.

[42]   Zeng, D., Ding, Z., Friedman, M. H., and Ethier, C. R., 2003, "Effects of Cardiac Motion on Right Coronary Artery Hemodynamics.," Ann. Biomed. Eng., **31**(4), pp. 420–429.

Figure Captions List

Fig. 1   Stented left anterior descending coronary artery models. Case A was treated with a Xience Prime stent (Abbott Laboratories), Case B with two Endevour Resolute stents (Medtronic), and Case C with the Magmaris bioresorbable scaffold (Biotronik AG). Stent strut malapposition is present in Case A (red circle) while stent overlapping in Case B (black circle). The main flow direction is indicated by the black arrows. (Online version in color)

Fig. 2   Coronary artery stents implanted in the three patient-specific vessels under investigation: Case A) single Xience Prime stent (Abbott Laboratories); Case B) two Endeavor Resolute stents (Medtronic) with an overlapped region; Case C) single Magmaris bioresorbable scaffold (Biotronik AG). A cross-sectional view of the stents is shown on the left. A magnification of the stents, highlighting their specific design, is depicted on the right

Fig. 3   A) Explanatory sketch of the topological features of the wall shear stress (WSS) vector field, showing a possible configuration of WSS contraction/expansion regions (colored by blue/red respectively), identified by negative/positive values of divergence of the normalized WSS vector field $\mathrm{DIV_{WSS}}$. The associated fixed points, which can be different in terms of type (i.e., saddle points, nodes, foci) and nature (i.e.,

stable, unstable), are also displayed. B) Schematic representation of the
contraction/expansion action exerted by the WSS on the cells in contact
with the blood flowing through the coronary artery. (Online version in
color)

Fig. 4   Color maps of the through-plane velocity component superimposed to
streamline visualization of the in-plane velocity at peak flow rate on
explanatory cross-sections of the three cases under investigation. (Online
version in color)

Fig. 5   Topological skeleton of the cycle-average WSS vector along the luminal
surface of the three cases under investigation. Contraction and
expansion regions, identified by negative and positive values of the
divergence of the normalized WSS vector field DIV_{WSS}, are indicated in
blue and red, respectively. The location of the fixed points (i.e., saddle
points and foci/nodes) over the luminal surface of the coronary arteries
is also shown. +ve: positive; -ve: negative. (Online version in color)

Fig. 6   Color maps of topological shear variation index (TSVI) along the luminal
surface of the three stented and non-stented cases under investigation.
(Online version in color)

Fig. 7   Violin plots of the values of topological shear variation index (TSVI) along
the luminal surface of stented region of the three cases under
investigation

Fig. 8   Color maps of time-averaged wall shear stress (WSS) along the luminal

surface of the three stented and non-stented cases under investigation.

(Online version in color)

Fig. 9   Violin plots of the values of time-averaged wall shear stress (TAWSS)

along the luminal surface of stented region of the three cases under

investigation

Fig. 10   Color maps of the divergence of the normalized WSS vector field DIV_{WSS},

topological shear variation index (TSVI), and time-averaged wall shear

stress (TAWSS) along the stent strut surface of the three cases under

investigation. Only a portion of the stents is visualized. For Case B, the

stent overlapping region is shown. The location of the fixed points (i.e.

saddle points and foci/nodes) over the stent strut surface is also shown.

The black arrows indicate the main direction of the flow. +ve: positive, -

ve: negative. (Online version in color)

Fig. 11   Explanatory sketch of the topological features of the wall shear stress

(WSS) vector field of a stented vessel portion. WSS contraction regions

(in blue), identified by negative values of divergence of the normalized

WSS vector field DIV_{WSS}, are located immediately upstream from the

stent struts. WSS expansions regions (in red), identified by positive

DIV_{WSS} values are located immediately downstream from the stent

struts. The possible location of the fixed points (i.e., saddle points and

foci/nodes) over the luminal surface is also shown. (Online version in color)

Table Caption List

Table 1   Number of fixed points identified in the three investigated cases

Table 2   Percentage increase in weighted fixed points area (wFPA), topological

shear variation area (TSVA), and low shear area (LSA) at the stented region
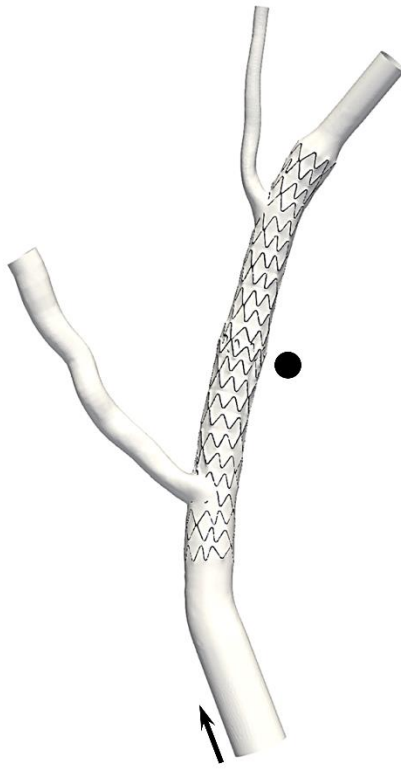
for the stented cases with respect to the non-stented ones

Tables

Table 1 Number of fixed points identified in the three investigated cases

	Case A	Case B	Case C
Stented models			
n. saddle points	432	717	201
n. foci/nodes	533	550	211
Non-stented models			
n. saddle points	1	3	2
n. foci/nodes	0	0	0

Table 2 Percentage increase in weighted fixed points area (wFPA), topological shear variation area (TSVA), and low shear area (LSA) at the stented region for the stented cases with respect to the non-stented ones

	Case A	Case B	Case C
Percent. increase in wFPA	165.47 %	440.16 %	71.07 %
Percent. increase in TSVA	680.87 %	603.23%	593.85%
Percent. increase in LSA	544.94 %	415.18 %	486.24 %

Figures

CASE A CASE B CASE C

Figure 1

CASE A
1 Xience Prime stent
(3.0x28 mm)

Square cross-section
(**81 μm**)

Open cell peak-to-valley

CASE B
2 Endeavor Resolute stents
(2.75x15 mm, 3.0x15 mm)

Circular cross-section
(**91 μm**)

Open cell peak-to-peak

CASE C
1 Magmaris bioresorbable scaffold
(3.0x25mm)

Rectangular cross-section
(**150 μm**)

Open cell peak-to-valley

Figure 2

Figure 3

Figure 4

Figure 5

Figure 6

Figure 7

Figure 8

Figure 9

CASE A

CASE B

CASE C

DIV$_{WSS}$ - ve   + ve

TSVI $_{(m^{-1})}$ 0 5×10^3

TAWSS $_{(Pa)}$ 0   2
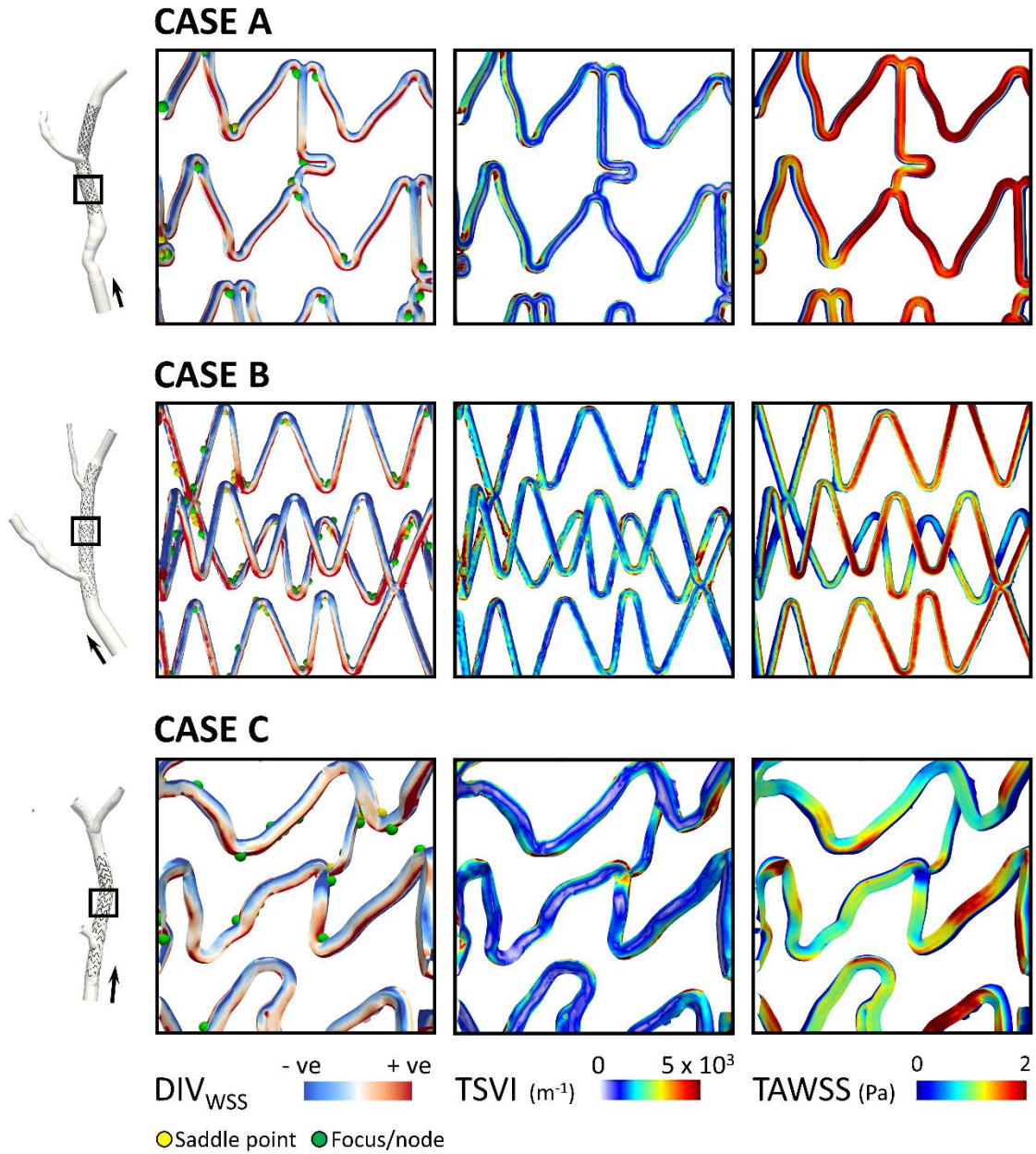
⬤ Saddle point   ⬤ Focus/node
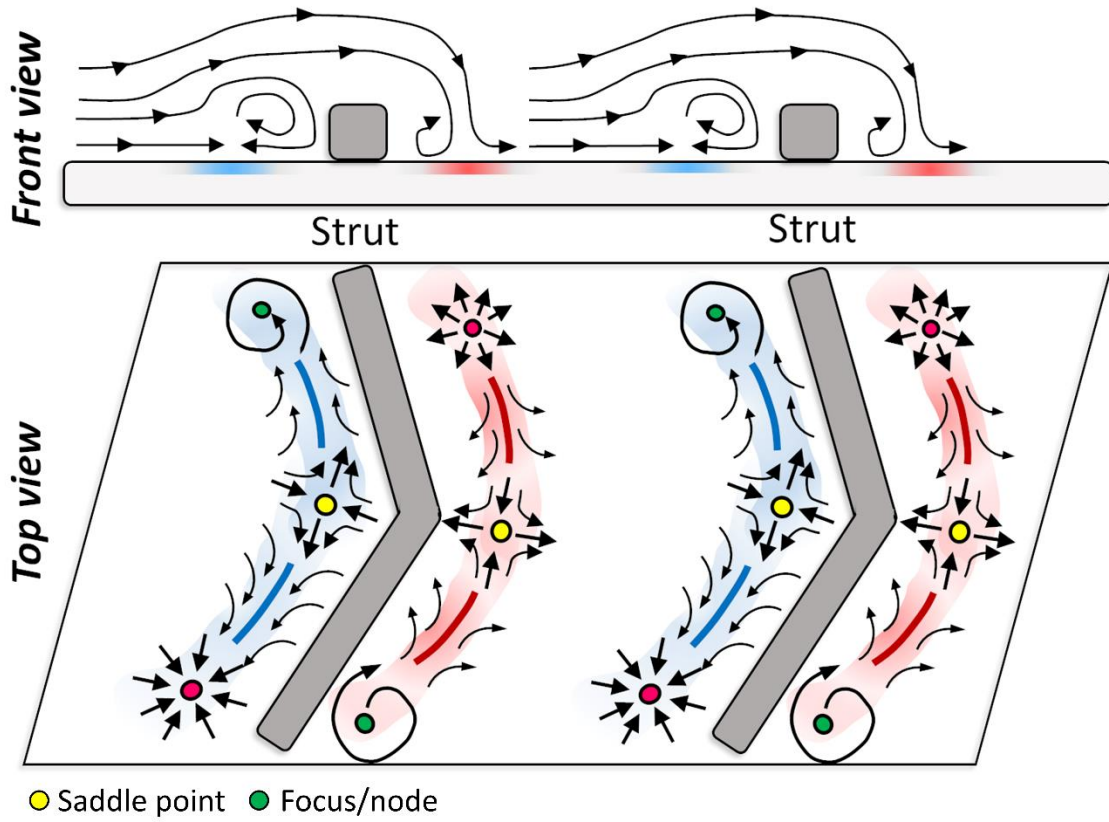
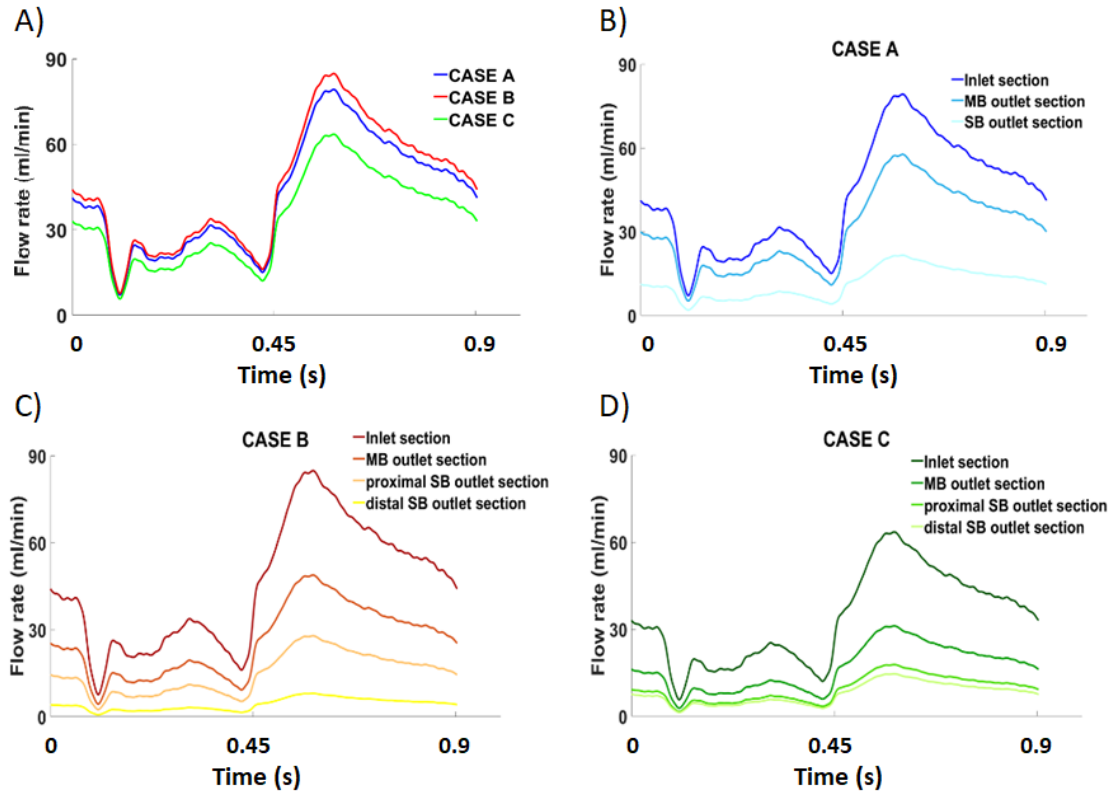**Figure 10**

Figure 11

SUPPLEMENTAL MATERIALS

Fig S1. A) Shapes of flow waveform that were applied at the inlet section of each model. Shapes of flow waveform applied at the inlet and outlet section of B) CASE A, C) CASE B and D) CASE C. MB: main branch; SB: side branch. (Online version in color)